PAPER

CrossMark
click for updates

A pH-responsive amphiphilic chitosan–pyranine core–shell nanoparticle for controlled drug delivery, imaging and intracellular pH measurement†

Hao-Syun Chou,[a] Meng-Hsuan Hsiao,[a] Wei-Yang Hung,[a] Tin-Yo Yen,[b] Hui-Yi Lin*[c] and Dean-Mo Liu*[a]

A pH-responsive multifunctional core–shell nanoparticle, named CHC–PY nanoparticle, was successfully synthesized through electrostatic interaction of a thin shell of fluorescent pyranine dye (PY) with amphiphilic carboxymethylhexanoyl chitosan (CHC) nanoparticles. Upon encapsulating an anticancer drug, camptothecin (CPT), the CHC–PY nanoparticles exhibited an excellent drug loading efficiency (>95%). The resulting CPT-loaded CHC–PY nanoparticles also exhibited efficient cell internalization and good pH-responsive behavior. After being internalized (*via* efficient endocytosis pathway), the presence of fluorescent PY shell showed a pH-dependent emission characteristic which allowed the internalized CHC–PY nanoparticles acting as an indicator to distinguish the acidic microenvironment of cancerous cells, compared with normal cells. The pH-sensitive PY shell also acted as a modulator to control the CPT release wherein a higher release rate was detected at lower pH value, which is essentially a potential therapeutic niche for anticancer purposes. This new type of CHC–PY core–shell nanoparticle provides multiple functionality, where a synergistic performance of nanotherapeutics, imaging and even diagnosis at a cellular resolution can be achieved simultaneously.

1. Introduction

One of the most challenging hurdles in the field of biological studies is the construction of the full picture for cancer progression and development. While most of the researches have focused on the investigation of enzymatic or genetic causes of cancer formation, very few have investigated the development of biomedical devices for detection and differentiation of cancer cells from normal cells. Intracellular pH is one of the most intriguing factors in initiating a cascade of cellular and physiological events, including apoptosis,[1] multi-drug resistance,[2] ion transport,[3] endocytosis,[4] and normal muscle contractions.[5] Abnormality in intracellular pH value is indicative for anomalous cellular function and growth, which often correlates to cancer cell development.[5–8]

Conventional methods of intracellular pH (pHi) measurement include microelectrodes,[9–11] NMR,[12,13] absorbance spectroscopy and fluorescence spectroscopy.[14–16] These methods have the advantages of spatial and temporal observations for pHi changes, high sensitivity, simple operation processes, and non-destructive to cells. 8-Hydroxypyrene-1,3,6-trisulfonic acid, also known as pyranine, has been used as a staining agent or pH indicator for cells or tissues.[17,18] The molecule is an exceptional pH indicator in several respects: water-soluble, superior chemical and physical stability,[19] high cellular retention, high pH sensitivity, pH-independence for ratiometric measurement, and easy imaging for both *in vivo* and *in vitro* studies. Nevertheless, when compared to other pH indicating molecules such as BCECF, BCPCF, and 1,4-DHPN,[20–22] pyranine exhibits poor cellular internalization. Most often the internalization of pyranine or other pH indicators is achieved through invasive methodologies, such as microinjection, electroporation, and scrape-loading.[23] While effective, these methods cause cell damages that may contribute to inaccuracy in pH determination. Thus, alternative cellular internalization methods with less detrimental outcomes, such as endocytosis, are required for more efficient and precise measurement of cellular pH and other therapeutic modalities.

Over the past few decades, developments of multifunctional nanocarriers with combined functionalities, such as

[a] Department of Materials Science and Engineering, National Chiao Tung University, 1001 Ta-hsueh Rd., Hsinchu, Taiwan. E-mail: deanmo.liu@gmail.com; hylin@mail.cmu.edu.tw; Tel: +886-3-5712121 ext. 55391

[b] Joint Honours of Biotechnology, Department of Microbiology and Immunology, University of British Columbia/British Columbia Institute of Technology, Vancouver, Canada, V6T 1Z4

[c] School of Pharmacy, China Medical University, TaiChung, Taiwan

† Electronic supplementary information (ESI) available. See DOI: 10.1039/c4tb01080a

6580 | *J. Mater. Chem. B*, 2014, **2**, 6580–6589

This journal is © The Royal Society of Chemistry 2014

cell-specific delivery, intracellular imaging, and hyperthermia therapy, have gradually matured in biomedical engineering.[24–27] Several *in vivo* evaluations have investigated the effectiveness of various multifunctional nanostructures proposed in the past, and demonstrated correlations between multifunctional nanostructures and improved therapeutic performances.[24,28] However, it has been relatively rare and challenging to synergize nanocarriers that enables both monitoring of intracellular pH and triggered drug release upon a change of physiological pH within normal cells, tumors, or diseased tissues. Therefore, it is important and of great interest to develop novel nanoparticles that are capable of delivering various therapeutic modalities, while providing stability and functionality for pH measurement under specific microenvironment (*e.g.*, acidic within cancerous cells) upon rapid cellular internalization.

Here, we report a pH-responsive multifunctional drug delivery nanosystem, which was successfully synthesized through a facile interaction of pyranine (PY), forming the shell phase, with an amphiphilic chitosan, carboxymethylhexanoyl chitosan (CHC), as the core phase. This new type of core–shell nanoparticle, termed CHC–PY, demonstrated excellent cytocompatibility, pH-responsive drug release behavior, and intracellular internalization efficiency for both cancerous and normal cells.[29–32] The electrostatic force between the negatively charged PY shell and positively charged CHC core allowed the core–shell nanostructure to be built efficiently while the outer shell of PY is tunable in thickness to modulate the drug release profile and emission intensity upon external excitation (Scheme 1). This work reports a successful design of such a core–shell nanoparticle capable of delivering an anticancer drug in a pH-sensitive manner and, at the same time, allowing *in situ* detection of intracellular pH of various cell lines upon efficient cellular internalization. Besides, the fluorescent emission intensity of the PY shell is of a pH-dependent nature which enables the resulting core–shell CHC–PY nanosystem to act as an imaging and potential diagnosis agent used to differentiate normal cells and cancer cells through their distinct intracellular physiological pH condition, which renders this new type of

CHC–PY nanoparticle a potential multifunctional platform for biomedical uses.

2.   Materials and methods

2.1.   Materials

The synthesis of amphiphilic CHC was reported previously and has been described in detail in a number of publications from our lab.[29,30] The hydrophobic hexanoyl group and hydrophilic carboxymethyl group allow the CHC molecules to self-assemble in neutral aqueous medium into nanoparticles of 100–200 nm in diameter, giving rise to a positively charged colloidal geometry in the resulting CHC nanoparticles. Pyranine was bought from Tokyo Chemical Industry and was used as received without further purification. The anticancer drug (*S*)-(+)-camptothecin (CPT) (M_n = 348.36, approx. 95% (HPLC)) was purchased from Sigma-Aldrich and used as received.

2.2.   Preparation of CHC–PY nanoparticles

10 mg CHC powder was first dispersed in 5 mL distilled water. The solution was gently shaken at room temperature for 24 h, and then sonicated using an automatic ultrasonic processor, UH-500A (China), at 35 W for 30 s. Pulse function with 5.0 s intervals and 1.0 s intervening pulse-off period was used during sonication to prevent build-up of excessive heat. The sonication process was repeated three times until an optically clear solution was obtained. According to previous studies, the amphiphilic CHC macromolecules self-assemble into spherical nanoparticles with an average size of 100–150 nm in diameter after dispersing in aqueous solution. The stabilized colloidal CHC nanoparticles possess a positive surface charge of 34.3 ± 0.7 mV, which allows for deposition of the negatively charged PY molecules (−6.6 ± 1.3 mV) to form a corona phase surrounding the CHC core *via* strong electrostatic interaction.

Pyranine solutions (5 mL) at concentrations ranging from 0.1 mg mL^{-1} to 0.3 mg mL^{-1} were prepared and added in a drop-wise fashion into aliquots of CHC colloidal samples with a fixed concentration of 1 mg mL^{-1}. The mixtures were stirred at room temperature for 1 h, and then centrifuged at 12 000 rpm for 10 min at 20 °C, from which the precipitates were decanted to obtain CHC–PY nanoparticles. The amount of pyranine adsorbed onto the CHC–PY nanoparticles was analyzed by measuring the UV absorbance of the supernatant that contained free pyranine, the measured value of which was then used to calculate the amount adsorbed onto the CHC nanoparticles. The wavelength of pyranine absorption in the UV spectrum is at 460 nm, and the supernatant was diluted in pH 7 phosphate-buffered saline (PBS) buffer to control the pH value of the solution.

2.3.   Preparation of drug-loaded nanoparticles

Drug entrapment into CHC–PY nanoparticles was carried out using the following procedures. Dimethyl sulfoxide (DMSO, reagent grade, Sigma Inc.) was used as a co-solvent to dissolve the hydrophobic drug CPT, and the solution was diluted with deionized (DI) water (0.5/9.5 v/v) to reach a working
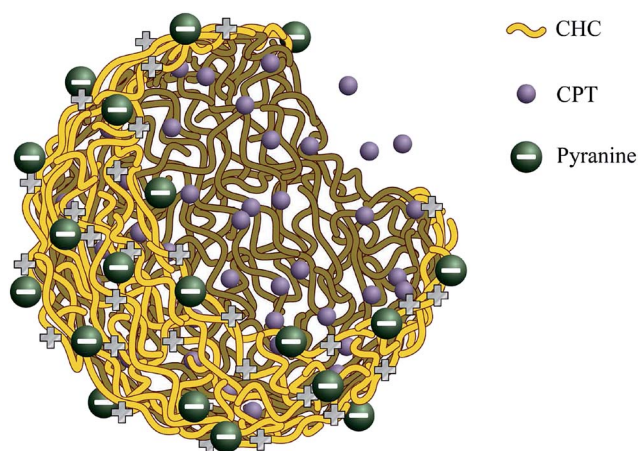
Scheme 1   The structure of CHC–PY nanoparticle.

CHC

CPT

Pyranine

concentration of 100 μg mL^{-1}. Then, powdered form of CHC was added to the solution until a final concentration of 2 mg mL^{-1} CHC was achieved. The mixture was stirred at ambient temperature for 24 h for formation of CHC nanoparticles and efficient drug encapsulation. After preparation of CPT-loaded nanoparticles, pyranine solutions of different concentrations were added to aliquots of CPT-loaded nanoparticle suspensions, and stirred at room temperature for 1 h. The solutions were then centrifuged at 20 °C at 2000 rpm for 5 min, followed by another cycle at 12 000 rpm for 10 min to obtain final CPT-loaded CHC–PY nanoparticles.

Concentration of free CPT (not being encapsulated) in the supernatant of each solution was measured in triplicate using high performance liquid chromatography (HPLC, Agilent Technologies 1200 Series) at a wavelength of 367 nm, a characteristic absorption band of CPT. The measurement was carried out using a 150 mm × 4.6 mm C18 column of 5 μm in diameter, with a constant flow rate of 0.8 mL min^{-1}. The mobile phase was composed of a DI water aqueous phase (A) and an acetonitrile organic phase (B), in a volume ratio of A : B = 3 : 2 (v/v). Drug encapsulation efficiency (EE) can be calculated using the following equation:

$$EE = \frac{(A - B)}{A} \times 100\% \qquad (1)$$

where A is the total amount of CPT and B is the amount of CPT remaining in the supernatant.

2.4. Characterization of CHC–PY nanoparticles

The surface charge of CHC–PY nanoparticles was characterized *via* zeta potential (Delsa Nano C, Beckman Coulter, USA) at pH 6. Particle size was measured using dynamic light scattering spectroscopy (DLS, BI-200SM Goniometer DLS, Brookhaven Inc., Holtsville, NY), and structural images were acquired using transmission electron microscopy (TEM, JEOL2100, Japan) with voltage of 200 keV for optimal imaging quality. TEM samples were prepared by soaking a carbon-coated copper grid in CHC–PY solution and then drying at room temperature.

2.5. CPT release behavior

Drug release behavior from the CPT-loaded CHC–PY nanoparticles was determined by measuring the concentration of CPT in 1 mL PBS solution at different release conditions and time durations. After centrifugation at 8000 rpm, the supernatant that contained the released drug was subjected to HPLC detection at a wavelength of 367 nm for CPT measurement. Each CPT concentration was obtained from triplicate measurements.

Drug release profiles of the CHC–PY nanoparticles were further analyzed using the power law equation:[33,34]

$$\frac{M_t}{M_\infty} = Kt^n \qquad (2)$$

where M_t/M_∞ is the percent of the drug released at time t, K is a rate constant incorporating structure and geometric

characteristics of the release device, and n is a characteristic exponent indicative of the release mechanism.

2.6. *In vitro* cytotoxicity and therapeutic efficacy

Lung adenocarcinoma cells (A-549) were cultured in 96-well culture plate with 1×10^4 cells for 24 hours before treatment. 2 mg mL^{-1} CHC–PY0.2 nanoparticles, 2 mg mL^{-1} CPT-loaded CHC–PY0.2 nanoparticles, and 192.2 μg mL^{-1} free CPT were added, separately. After incubation for 24 hours, MTT solution (0.5 mg mL^{-1}) was added and reacted for 4 hours. Then, DMSO was added to dissolve the purple formazan which was measured by a MicroELISA reader (GDV, DV 990BV4, Italy) at 595 nm. Cell viability was determined by calculation according to the following equation:

$$\text{Cell viability (\%)} = (A_{sample}/A_{control}) \times 100\%$$

where A_{sample} is the absorbance of sample and $A_{control}$ is the absorbance of control.

2.7. Intracellular pH determination

Three cell lines of human origin were cultured in order to investigate the intracellular pH value with different oncological statuses: intestinal epithelial cells (IEC-6), representing normal cells, and heterogeneous human epithelial colorectal adeno-carcinoma cells (CaCo-2) and lung adenocarcinoma cells (A-549), representing cancer cells. 1×10^6 cells of each of these cell lines were first cultured in a 10 cm cell culture dish. The cultures were then incubated overnight with an addition of 4 mg mL^{-1} CHC–PY nanoparticle solutions. The cells were then harvested and re-suspended in 1 mL of DI H$_2$O, and the suspensions were measured for UV absorbance at characteristic wavelengths of 460 and 405 nm. Correction for the signal value, R_{ex}, was calculated using the following formula:

$$R_{ex} = (\lambda_{exc.\ 460\ nm}/\lambda_{exc.\ 405\ nm}) \qquad (3)$$

The calculated values of R_{ex} were further converted to $\log(R_{ex})$ using the following formula:

$$\log(R_{ex}) = 0.398x - 2.983 \qquad (4)$$

where x is the intracellular pH value (ESI Fig. S1†). The conversion allowed for the analysis of logarithmic correlations between sample absorbance and both extracellular pH and intracellular pH.

3.8. Intracellular imaging

Both IEC-6 and CaCo-2 cell lines were employed as model cells representing normal and cancer cells, respectively, to evaluate the imaging capability of the CHC–PY nanoparticles. Cells were cultivated on glass coverslips for 24 h, and treated with 0.1% (w/w) CHC–PY nanoparticles for different incubation durations. After washing with PBS to remove excess nanoparticles, the cells were mounted on fresh glass slides, and analyzed with a multiphoton and confocal microscope system (MCMS) (TCS-SP5-X AOBS, Leica, Mannheim, Germany) with 470 nm laser

6582 | *J. Mater. Chem. B*, 2014, **2**, 6580–6589

This journal is © The Royal Society of Chemistry 2014

Table 1 Physical characteristics of CHC–PY nanoparticles and drug encapsulation efficiency with different CHC–PY ratios. The numbers of sample ID, namely 0.1, 0.15, 0.2, and 0.3, mean the pyranine concentration of the prepared solutions

Sample ID	PY deposition [$\mu g\ mL^{-1}$]	Zeta potential [mV]	Mean size [nm]	Encapsulation efficiency [%]
CHC	0	34.3 ± 0.7	107.7 ± 1.9	90.7
CHC–PY0.1	70.4 ± 3.6	32.1 ± 1.4	113.5 ± 2.9	95.4
CHC–PY0.15	119.9 ± 3.8	25.3 ± 2.3	119.6 ± 1.5	95.8
CHC–PY0.2	162.2 ± 6.2	18.5 ± 2.7	123.7 ± 2.7	96.1
CHC–PY0.3	260.4 ± 7.2	8.7 ± 1.8	132.6 ± 0.5	96.5

excitation and 405 nm UV light excitation. The ratio of I_{405}/I_{470} was determined by the averaged values (in quadruplicate measurements) of measured emission intensity of Ex 470 and Ex 405, where the difference in the ratio can be easily distinguished between normal cells and cancer cells due mainly to the difference in respective intracellular pH value.

3. Results and discussion

3.1. Pyranine shell formation on CHC nanoparticles

Electrostatic attraction between negatively charged pyranine and positively charged CHC nanoparticles was responsible for the formation of CHC–PY core–shell nanoparticles. Calculations of pyranine deposition were based on the UV spectrum of the supernatant after centrifugation. The amount of pyranine deposited onto the surface of CHC nanoparticles was dependent on the concentration of pyranine added into the CHC solution; an increasing trend in pyranine deposition with increasing pyranine concentration was observed (Table 1). Such phenomenon was believed to be the result of pyranine deposition equilibrium, which would be driven towards deposition as the concentration of added pyranine increased. This ultimately led to higher coverage of pyranine on the surface of CHC cores, and gave rise to a decreased zeta potential and an increased size of the resulting CHC–PY nanoparticles (columns 3 and 4 in Table 1).

3.2. Colloidal properties of CHC–PY nanoparticles

The effect of pyranine on zeta potential and mean size of the CHC–PY nanoparticles was investigated using samples prepared with different pyranine concentrations. The zeta potential of resulting CHC–PY nanoparticles, as given in Table 1, decreased with increasing concentration of pyranine. This observation was a result of charge neutralization between the positively charged CHC surface and negatively charged pyranine upon deposition. As mentioned above, when the total contributed charge of pyranine intensifies, the amount of deposited pyranine on the CHC nanoparticles increases. This leads to two outcomes, both of which contribute to the decrease in zeta potential of CHC–PY nanoparticles: (a) the shielding of the positive charge of the CHC nanoparticle core by the negatively charged pyranine, and (b) gradual decrease in overall positive charge from 34.3 mV to 8.7 mV as the pyranine concentration increases from 0 to 0.3 mg mL^{-1}. This means that the emission intensity and nature of the CHC–PY nanoparticles are highly

tunable, leading to a broad spectrum of colloidal properties of the nanoparticles that can potentially be utilized for a range of biomedical applications.

The sizes of the final CHC–PY nanoparticles determined using DLS (Table 1) were 107 nm, 113 nm, 120 nm, 124 nm and 133 nm as the pyranine increased from 0 mg mL^{-1}, 0.1 mg mL^{-1}, 0.15 mg mL^{-1}, 0.2 mg mL^{-1} to 0.3 mg mL^{-1}, respectively. These values corresponded to an average thickness of the pyranine shells ranging from 0 nm, 3 nm, 6.5 nm, 8.5 nm to 13 nm, respectively. A linear correlation between shell thickness and
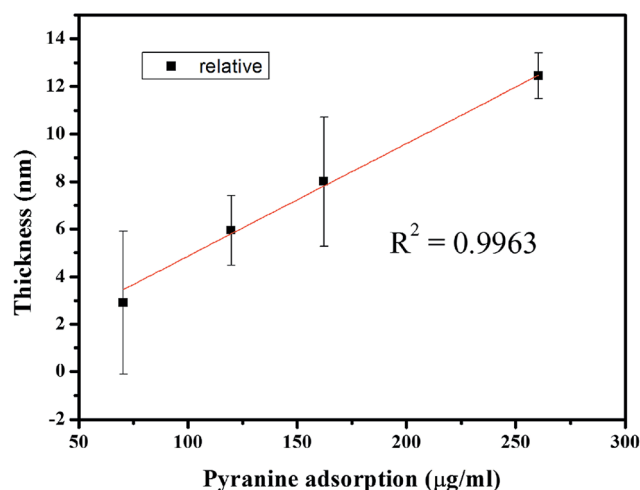
Fig. 1 The pyranine shell thickness increases linearly with increasing amount of pyranine deposited on the CHC core.
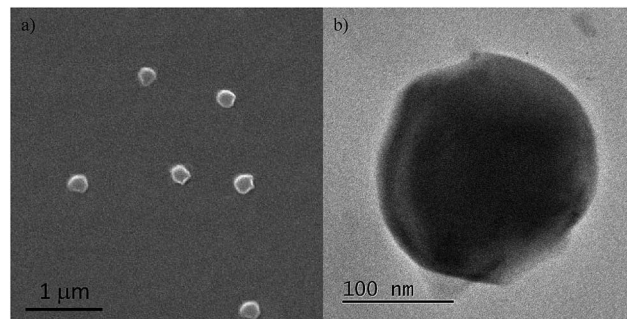
Fig. 2 Morphology of CHC–PY nanoparticles: (a) SEM image of self-assembled CHC nanoparticles and (b) TEM image of CHC–PY0.2 nanoparticle, showing a pyranine shell after rapid electrostatic deposition.

pyranine concentration, as shown in Fig. 1, was observed and was indicative of zero-order pyranine deposition kinetics that followed a relatively constant electrostatic-dominated mechanism. Since the molecular size of pyranine is approximately 1.5 nm and it has a bulky shape, it was then estimated that the formed shell could be composed of 2, 4, 6, and 9 layers of deposited pyranine by the assumption of a uniform deposition throughout the shell-forming process. Since the CHC core is nearly spherical in shape as shown in Fig. 2a, TEM examination was used to confirm the presence of a core and outer shell layer in the CHC–PY0.2 nanoparticle sample, as shown in Fig. 2b. The image indicated the pyranine was successfully deposited on the surface of the CHC core in a random fashion, with patches of the shell being slightly thicker than the rest of the nanoparticle surface. While the underlying reason for the unevenness of pyranine deposition along the core surface is unclear, we postulated that the strong positive charge exhibited by the non-coated CHC core favors a fast non-homogeneous pyranine distribution at the beginning of the coating process. As more pyranine is brought to the quick-forming CHC–PY nanoparticles, the electrostatic attraction exerted by the CHC–PY surface becomes weaker, thus resulting in a more gradual deposition of pyranine until the deposition equilibrium is reached.

3.3. Structural stability of pyranine shell

Once the pyranine molecules were successfully deposited onto the CHC core, it became critical to investigate the stability of the deposited pyranine, since the electrostatic attraction force provided the necessary energy for non-covalent bonds between the CHC and pyranine molecules. The bonds may suffer from breakage in the form of pyranine desorption in dilute environments (i.e. the circulatory system) or long-term shelf storage. This may further lead to a change in properties such as spectral emission intensity, drug release profile due to decreasing surface coverage, surface net charge and more, which ultimately weaken the desired performance of the encapsulated drugs. Therefore, characterization of the pyranine shell stability is absolutely essential to ensure the practical niche of the resulting core–shell nanoparticle. The amount of pyranine adhering to the surface of the CHC nanoparticle under different pH environments was evaluated by UV spectroscopy. Diluted media of different pH values, as well as different collection time periods of 0, 0.5, 24, and 120 h, were selected to carry out the investigation.

The third column of Table 2 provides the amount of pyranine remaining on the CHC core that was detected after the first 30 min in the dilution test, with a starting pyranine concentration normalized as 100% ($t = 0$, second column). 2% of remaining pyranine (from 100% reduced to 98%) was measured at pH 4, and 7% (100% → 93%) at pH 5, 14% (100% → 86%) at pH 6, and 21% (100% → 79%) at pH 7 were measured. Such a trend clearly revealed pyranine desorption from the CHC–PY nanoparticles. However, the desorption rate declined significantly over a subsequent duration of nearly 120 h across all pH values, with only 5% (98% → 93%) at pH 4, 5% (93% → 88%) at pH 5, 6% (86% → 80%) at pH 6, and 8% (79% → 71%) at pH 7. This implied that the remaining pyranine molecules were structurally stabilized on the CHC core surface. This suggests that the initial pyranine desorption during the first 30 minutes is fast and dependent on the environmental pH. The surface charge of CHC core becomes weaker as the solution pH increases with larger dilutions (IEP is close to pH 7.5 for the CHC core nanoparticle, see Fig. S2†), which in turn reduces the electrostatic interaction between the CHC core and pyranine shell until sufficient amount of pyranine has been diluted. This loss of electrostatic attraction force causes the adhered pyranine to leave the CHC–PY nanoparticles, leading to the reduction of outer shell thickness, as well as the positive addition of the overall surface charge. As the surface charge of CHC–PY nanoparticles increases with reducing outer shell thickness, the shielding effect brought by the outer shell weakens and allows for even higher stability for the electrostatic attractive force between the remaining adhered pyranine and the CHC core. Thus, the stabilization between pyranine outer shell and CHC core is achieved through the increase of electrostatic attraction force; the pyranine molecules found on the outermost region of the shell are subjected to a reduced force of electrostatic attraction, making them less likely to stay adhered upon a change toward more basic pH.

In comparison to the initial pyranine desorption stage, further desorption of the adhered pyranine during the subsequent 120 h observation period was more gradual and less pronounced. This was especially prevalent at higher pH values, which indicated that the pyranine molecules adhered firmly on the core surface. This observation confirmed the use of pyranine to create a stable shell structure with great potential for biomedical applications.

3.4. Anticancer drug encapsulation

Once the stability of the pyranine shell was experimentally confirmed, the applicability of the resulting CHC–PY nanoparticles for drug delivery was evaluated using a highly hydrophobic drug, CPT, as the model molecule. The encapsulation efficiency of CPT was optimized at >95% for all CHC–PY compositions prepared in this work as given in Table 1. It is interesting that, in comparison with pure CHC core, higher drug loading efficiency was achieved with increasing pyranine deposition. One plausible reason was the fast surface coverage by pyranine upon mixing the CPT-containing CHC core and pyranine, wherein a shell was readily built up with increasing

Table 2 Remaining amount (normalized) of pyranine staying on the nanoparticle at different pH values for various time intervals (t) of incubation

pH value	$t = 0$ [%]	$t = 0.5$ h [%]	$t = 24$ h [%]	$t = 120$ h [%]
4	100	97.62	95.24	92.86
5	100	92.77	90.36	87.95
6	100	86.08	82.28	79.75
7	100	78.75	75.00	71.25
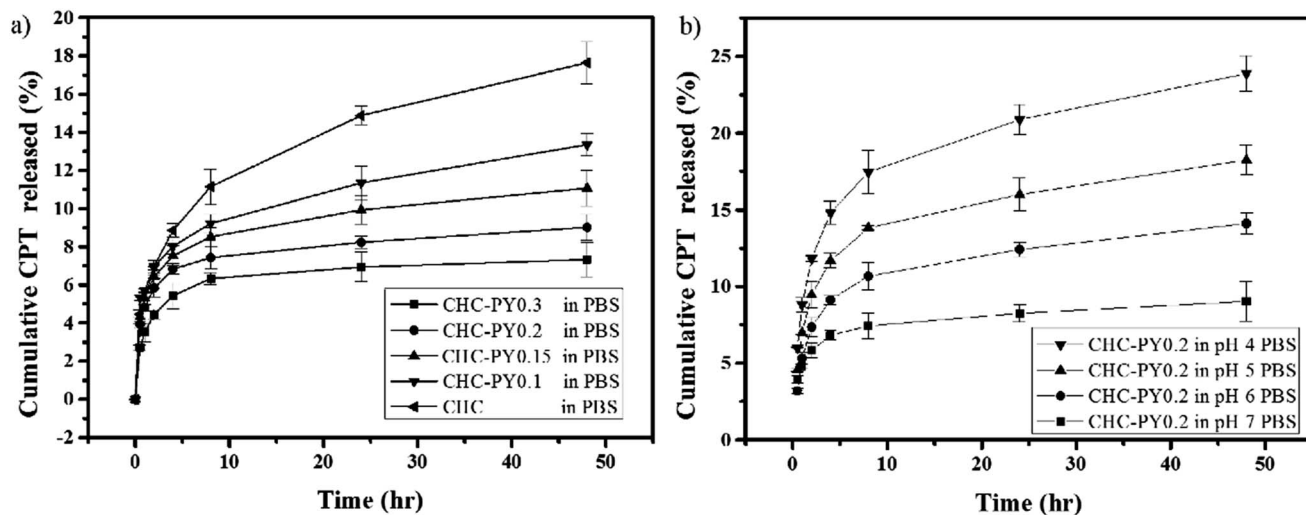
Fig. 3 (a) The release profile of CPT (0.1 mg mL^{-1}) from various pyranine concentrations (0.1, 0.15, 0.2, 0.3 mg mL^{-1}) in PBS solution. (b) The release profile of CHC–PY0.2 with CPT (0.1 mg mL^{-1}) from PBS buffer with different pH values (4, 5, 6, and 7).

thickness as pyranine increased, to form an effective barrier to inhibit the early-phase release of the CPT (see forthcoming section), resulting in a higher drug payload. This finding indeed gives a synergistic benefit to the multifunctional drug delivery system currently prepared, where higher drug payload and effective barrier for controlled drug delivery can be achieved synergistically.

3.5. Drug release behavior

3.5.1. Effect of pyranine concentration. Fig. 3a shows the resulting drug release profiles for the CPT-loaded CHC–PY nanoparticles prepared with various pyranine concentrations, from 0.1 mg mL^{-1} to 0.3 mg mL^{-1}, in PBS buffer of pH = 7. As expected, the release profile was significantly slower at higher pyranine concentrations, confirming the formation of a thicker pyranine shell that can effectively reduce the burst-like release of the CPT; instead, a slow and sustained release profile was achieved.

A closer examination on the release profiles of drug-loaded CHC–PY nanoparticles with lower pyranine concentrations, *i.e.*, 0.1 mg mL^{-1} and 0.15 mg mL^{-1}, revealed similar burst-elution behaviors to that observed in drug-loaded CHC core phase alone. We postulated that this could be due to the early-stage desorption of pyranine at higher solution pH (in this case, pH = 7), leading to a rapid thinning of the outer shell that allows CPT to leak through easily and elute into the diluting medium. However, the early-phase burst-like behavior can be effectively reduced by increasing the pyranine to more than 0.2 mg mL^{-1}, which is in good agreement with the previously mentioned analysis of the structural stability of the shell.

Also, the effect of pyranine shells on drug release kinetics can be evaluated from eqn (2), where the reaction order n of CHC–PY nanoparticles was determined experimentally to range from 0.16 to 0.20 (Table 3), suggesting a quasi-Fickian diffusion mechanism for the drug-loaded nanoparticles. The rate constant K was between 3.8 (CHC–PY0.3) and 6.0 (CHC–PY0.1), which demonstrated an inverse relationship with respect to increasing shell

thickness (Fig. 4). This trend further confirmed the inhibitory effect of pyranine outer shell on CPT elution *via* the increase in diffusion path length for the drug molecules to travel through.

3.5.2. Effect of solution pH. The influence of solution pH on the CPT release profile was examined using CHC–PY0.2 as a representative example, since this composition demonstrated high stability of the pyranine shell over a wide range of pH values. Fig. 3b shows the CPT release profiles at various pH values, ranging from 4 to 7. The rate of CPT release decreased with increasing solution pH, signifying a rapid release of CPT under acidic conditions and an inversely proportional relationship with solution pH up to near-physiological pH (pH 7). This pH-responsive behavior can be explained by two earlier observations: (a) at higher pH, the shell thickness reduced as a result of early-stage desorption, *i.e.*, *ca.* 20% pyranine loss at pH = 7, which corresponded to *ca.* 8% reduction of shell thickness, and (b) the surface charge of the CHC approached neutral. Both of these factors contributed to a more compact CHC core structure, resulting in a significant synergistic reduction of the CPT adhesion and coverage.

In contrast to the significant loss of adhered CPT in acidic environment, the reduction in shell thickness at lower pH was less. However, an observable swelling of the CHC core was noted, and was postulated to be as a result of intra- and inter-molecular repulsion due to the protonation of the amine groups

Table 3 Kinetic parameters: reaction order (n) and rate constant (K), obtained as a result of model fitting for the CPT release from CHC–PY nanoparticles with various starting pyranine concentrations

Sample	n	K	R^2
CHC	0.29 ± 0.01	5.88 ± 0.19	0.9949
CHC–PY0.1	0.21 ± 0.01	5.97 ± 0.08	0.997
CHC–PY0.15	0.19 ± 0.01	5.51 ± 0.19	0.9755
CHC–PY0.2	0.16 ± 0.02	5.04 ± 0.23	0.9399
CHC–PY0.3	0.18 ± 0.03	3.83 ± 0.28	0.9018

This journal is © The Royal Society of Chemistry 2014

J. Mater. Chem. B, 2014, **2**, 6580–6589 | **6585**
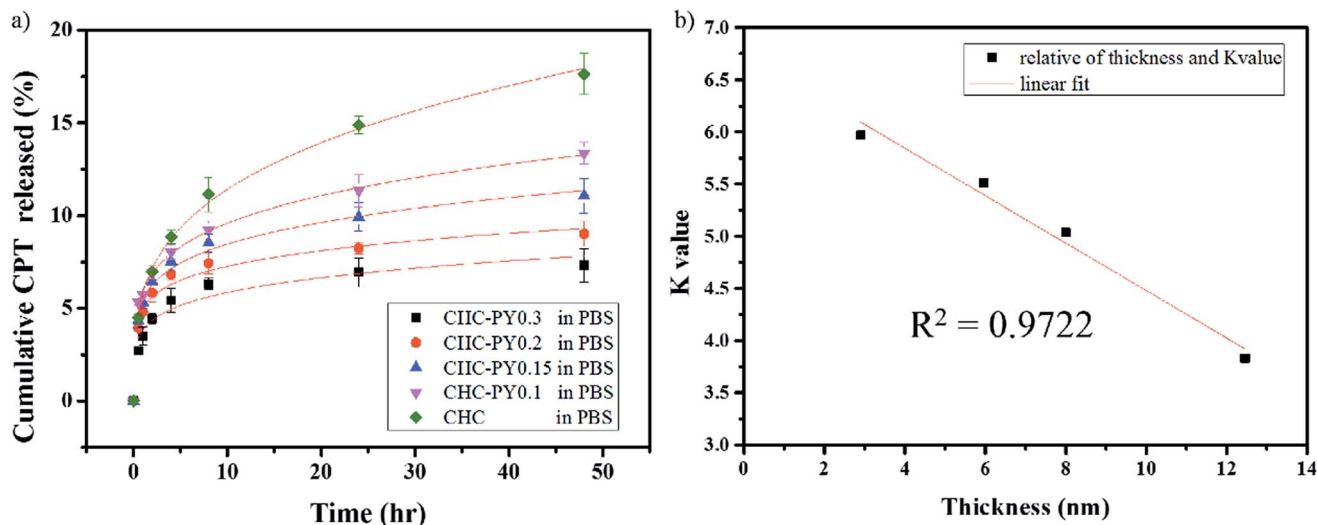
Fig. 4 (a) The release kinetics for various pyranine concentrations. (b) The rate constant decreases linearly with increasing pyranine shell thickness.

found in CHC. It appears, as shown in Fig. 3b, that the repulsion-induced swelling became more pronounced with decreasing pH, which corresponded to a simultaneous decrease in the drug release. We then conclude that the pH-responsive release behavior of CPT from the CHC–PY nanoparticles is virtually an interplay of pH responsiveness between the pyranine shell and CHC core. The nanoparticles appear to be a highly promising nanoplatform for anticancer therapeutics, as a higher drug release rate in acidic environment is more therapeutically favorable since some cancerous cells or tumors have been recognized to be more acidic in the intracellular microenvironment.[35]

3.6. *In vitro* cytotoxicity and therapeutic efficacy

The cytotoxicity of CHC–PY nanoparticles and their therapeutic efficacy were evaluated with A549 cells by MTT assay for 24
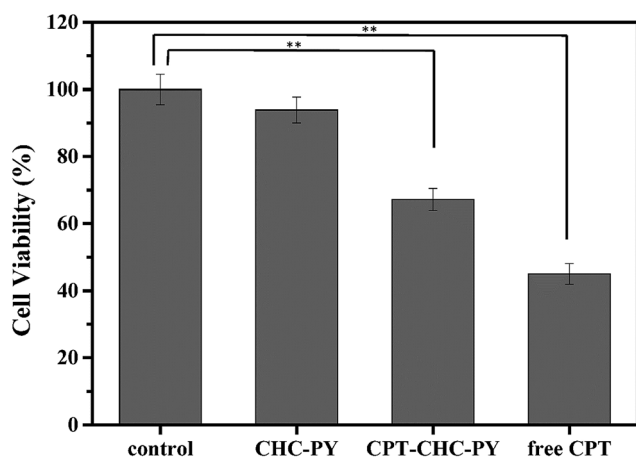
Fig. 5 Cell viability of A549 cells incubated with 2 mg mL^{-1} CHC–PY0.2 nanoparticles, 2 mg mL^{-1} CPT–CHC–PY0.2 nanoparticles (the total quantity of CPT in the nanoparticle is 192.2 µg mL^{-1}) free CPT for 24 hours ($n = 3$).

hours. As shown in Fig. 5, the viability of A549 cells treated with CHC–PY0.2 nanoparticles still remained above 90%, which is evidence that the nanoparticles have good biocompatibility and low cytotoxicity. The CPT-loaded CHC–PY0.2 nanoparticles (CPT–CHC–PY) and free CPT drug showed 70% and 50% cell viability, respectively. The concentration of free CPT was controlled to be the same concentration as that in CPT–CHC–PY nanoparticles to evaluate the therapeutic efficacy of the nanoparticles. The difference of therapeutic efficacy is due to the slow release property of CPT–CHC–PY nanoparticles. These evidences indicate that the CPT–CHC–PY nanoparticle is good candidate for loading hydrophobic anticancer drug and drug delivery because of its good compatibility and low toxicity.

3.7. Intracellular pH measurement

Intracellular pH is crucial in understanding many biological functions, including cell permeability, enzymatic activity, cell growth, cell differentiation, and cell apoptosis. In order to investigate the potential applicability of CHC–PY nanoparticles for the measurement of intracellular pH, as well as to study the intracellular behaviors of the nanoparticles in cancer cells and normal cells, normal cell line (IEC-6) and cancer cell lines (CaCo-2 and A549) were separately incubated with CHC–PY0.2 nanoparticles. Ratiometric probe was used to measure the excitation spectrum at wavelengths of 460 nm and 405 nm, and the ratios, or R_{ex} values, were calculated based on the measured primary maxima of the two wavelengths. As observed in the normalized excitation spectra of CHC–PY0.2 nanoparticles (Fig. 6a), an increase in buffer pH leads to an increase in the secondary maximum at 460 nm, which is the excitation wavelength of unprotonated pyranine. Meanwhile, the primary maximum at 405 nm, which is the excitation wavelength for protonated pyranine, remained relatively stable.

Fig. 6b shows the excitation spectra for the three cell lines, which are normalized to the maximum 405 nm peak. IEC-6

6586 | *J. Mater. Chem. B*, 2014, **2**, 6580–6589

This journal is © The Royal Society of Chemistry 2014
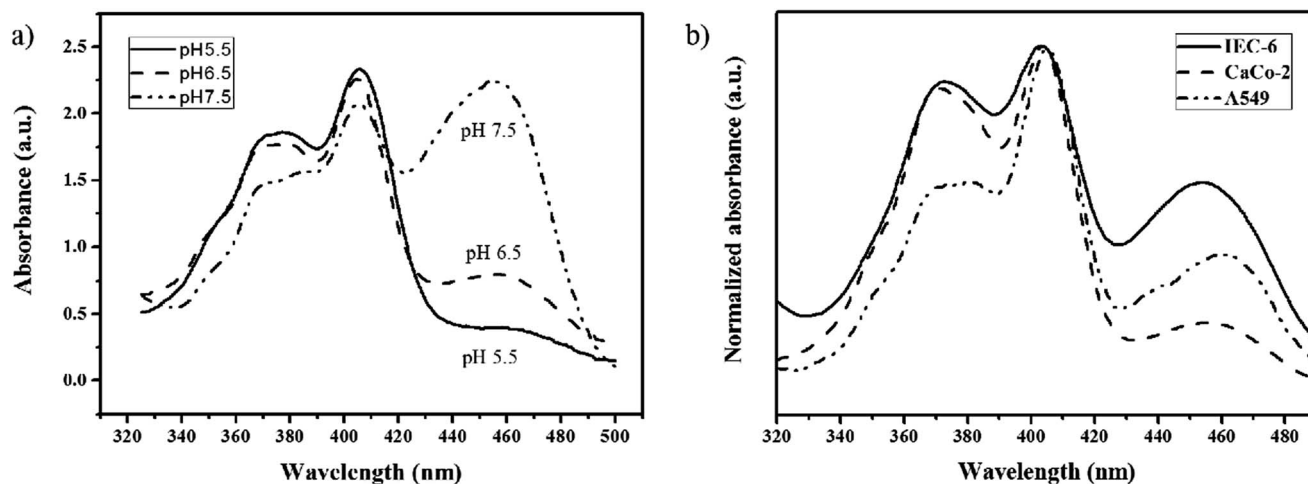
Fig. 6 Intracellular pH measurement with CHC−PY0.2 nanoparticles. (a) Normalized excitation fluorescence spectra of CHC−PY0.2 in buffer of pH 5.5, pH 6.5 and pH 7.5. (b) Fluorescence intensity of CHC−PY nanoparticles in different cell lines.

Table 4 Calculated pH values for three types of cell line

Cell line	Calculated pH value after 24 h incubation
IEC-6	7.02 ± 0.11
CaCo-2	6.30 ± 0.02
A-549	6.51 ± 0.06

showed the strongest absorbance at 470 nm compared with the other two cell lines, followed by CaCo-2 and A-549. This result indicated that the CHC–PY nanoparticles demonstrated an excellent and precise pH-responsive behavior in terms of normal cells and cancer cells *via* specific sensitizing of the intracellular pH value.

Results of the excitation spectra analysis were then compiled and calculated for both R_{ex} and $\log(R_{ex})$ of CHC–PY0.2 nanoparticles in different cell lines (Table 4). The calculated values of $\log(R_{ex})$ can then be used to approximate the pH value from the calibration graph. Calculated values indicated that the intracellular pH of IEC-6 was approximately 7.02, whereas CaCo-2 and A-549 appeared to be more acidic, with pH values of 6.30 and 6.51, respectively. The results are in excellent agreement with those of previous literature reports, and confirmed a highly pH-sensitized technique for monitoring the subtle variation in intracellular pH upon therapeutic treatment.[35–38]

The CHC–PY nanoparticles successfully predicted over a certain accuracy the intracellular pH value of normal cells (IEC-6) and cancer cells (CaCo-2 and A549). The pH-sensitive emitting nature of the fluorescent PY rendered the resulting CHC–PY nanoparticles capable of distinguishing the physiological microenvironment between cells of differing nature, to be specific, normal cells and cancer cells as used in this work, by their specific fluorescent emitting behavior. In Fig. 6b, the nanoparticles show a constant absorbance value at 405 nm for different pH levels but the absorbance varied at 470 nm. The intensity of the absorbance at 470 nm increased with the pH

value, which can be used as an indicator of distinct cells of various physiological natures *via* a simple cell culture protocol.

The CHC–PY nanoparticles internalized in IEC-6 and CaCo-2 were excited by λ_{ex} 405 nm and λ_{ex} 470 nm and the ratio of the emission intensity at 510 nm was calculated. As illustrated in Fig. 7, the emission intensity with λ_{ex} 405 nm is similar between IEC-6 and CaCo-2, but a notable difference is clearly detected between IEC-6 and CaCo-2 for λ_{ex} 470 nm. The emission intensity of the nanoparticles with IEC-6 was nearly 2.5-fold higher than that with CaCo-2, suggesting the capability of the CHC–PY nanoparticles in identifying the physiological difference between normal cells and cancer cells.

However, there was a problem as to whether the CHC–PY nanoparticles were in cytoplasm or organelles after endocytosis. Different locations of cells have different pH values greatly affecting the result of pH measurement, such as lysosome that is in a very acidic environment. From Fig. 6b, the spectra
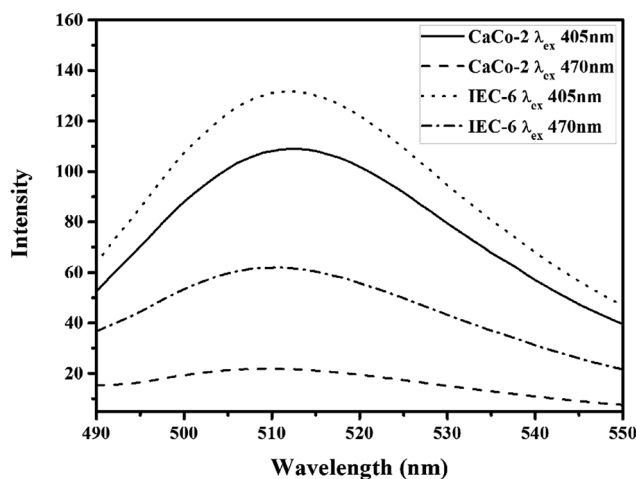
Fig. 7 The emission intensity of CHC-PY0.2 in IEC-6 cells or CaCo-2 cells measured with a fluorescence spectrophotometer. After normalizing with λ_{ex} 405 nm, the intensity of IEC-6 λ_{ex} 470 nm was higher than CaCo-2 λ_{ex} 470 nm by about 2.5 times.
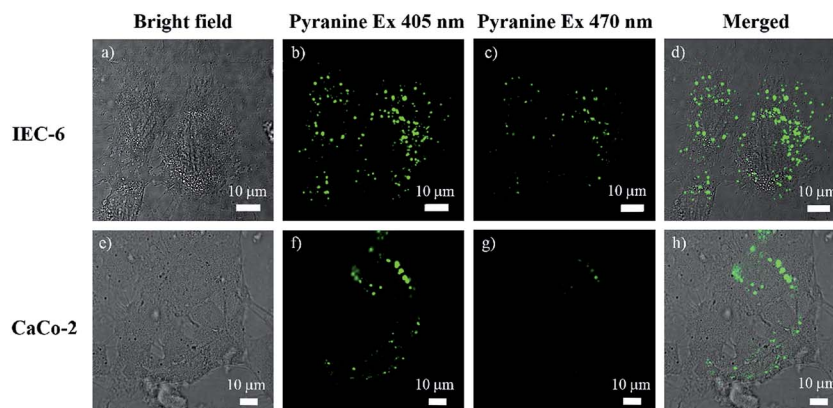
Fig. 8 Confocal microscope images of CHC–PY0.2 in IEC-6 cells (a–d) or CaCo-2 cells (e–h). (a and e) Bright field images of the two kinds of cells; (b and f) CHC–PY fluorescence images using 405 nm excitation; (c and g) using 470 nm excitation; (d and h) the merged image.

Table 5 The brightness value of different excitations and cells ($n = 4$)

Cell line	I_{405}	I_{470}	I_{405}/I_{470}
IEC-6	4.91	1.13	4.29 ± 0.50
CaCo-2	3.1	0.08	40.63 ± 2.96

showed macroscopic results that revealed what kind of environment the CHC–PY nanoparticles were in. From the macroscopic results, pH 7 for normal cells and pH 6.5 for cancer cells conformed to the results of other researches, which confirmed that the CHC–PY nanoparticles can measure correct intracellular pH values, and it was not dependent on which location of cells the CHC–PY nanoparticles were in.

3.8. Intracellular imaging

Besides their pH monitoring capability, the nanoparticles, after being internalized within the cells, were excited at 405 nm and a clear fluorescent image was visually detected, Fig. 8, indicating that the CHC–PY nanoparticles were highly accessible through the cell membrane by endocytosis while their fluorescent emitting behavior remained identical. The fluorescence intensity of nanoparticles in both IEC-6 cells and CaCo-2 cells was weakened when excited at 470 nm, as illustrated in Fig. 8c and g. However, the fluorescence intensity (brightness) of the nanoparticles in CaCo-2 cells was conspicuously lower than that in IEC-6 cells, which is virtually a result of the cell nature, as given in Table 5, where the value of I_{405}/I_{470} for IEC-6 (normal) cells and CaCo-2 (cancer) cells is 4.29 and 40.63, respectively. As a result, both the pH-dependent imaging contrast and pH monitoring capabilities mean that these CHC–PY nanoparticles could be a new multifunctional nanoplatform with enhanced nanomedicinal potential for a number of biomedical uses.

4. Conclusion

A pH-responsive multifunctional drug delivery nanoparticle was successfully synthesized by forming a core–shell nanostructure, composed of a CHC core and pyranine dye as a thin shell. The core–shell nanostructure exhibited a stable and tunable colloidal behavior in terms of size, surface charge, and fluorescence emission characteristics. The CHC–PY nanoparticles exhibited a strong synergizing performance with high drug encapsulation efficiency (>95%), efficient cellular internalization, pH-responsive drug release behavior, cell imaging capability, as well as the possibility of intracellular pH measurement. The pH-sensitizing property renders the CHC–PY nanoparticles a powerful indicator to distinguish the physiological pH nature between normal cells and cancer cells *via* fluorescence spectra and imaging modality. Such a new multifunctional nanoplatform allows a nanotherapeutic strategy to be tunable according to practical needs ranging from therapeutics to imaging to diagnosis or a combination therapy. Further investigation of the core–shell CHC–PY nanoplatform in terms of an animal model is under way which is intended to find niche performance toward better clinical translation.

References

1 D. Pérez-Sala, D. Collado-Escobar and F. Mollinedo, *J. Biol. Chem.*, 1995, **270**, 6235–6242.
2 S. M. Simon and M. Schindler, *Proc. Natl. Acad. Sci. U. S. A.*, 1994, **91**, 3497–3504.
3 A. Varadi and G. A. Rutter, *Endocrinology*, 2004, **145**, 4540–4549.
4 R. A. Gottlieb, J. Nordberg, E. Skowronski and B. M. Babior, *Proc. Natl. Acad. Sci. U. S. A.*, 1996, **93**, 654–658.
5 A. J. Bullock, R. A. Duquette, N. Buttell and S. Wray, *Pfluegers Arch.*, 1998, **435**, 575–577.

6588 | *J. Mater. Chem. B*, 2014, **2**, 6580–6589

This journal is © The Royal Society of Chemistry 2014

6 H. Izumi, T. Torigoe, H. Ishiguchi, H. Uramoto, Y. Yoshida, M. Tanabe, T. Ise, T. Murakami, T. Yoshida, M. Nomoto and K. Kohno, *Cancer Treat. Rev.*, 2003, **29**, 541–549.

7 T. A. Davies, R. E. Fine, R. J. Johnson, C. A. Levesque, W. H. Rathbun, K. F. Seetoo, S. J. Smith, G. Strohmeier, L. Volicer, L. Delva and E. R. Simons, *Biochem. Biophys. Res. Commun.*, 1993, **194**, 537–543.

8 J. Zhang, L. Wu, F. Meng, Z. Wang, C. Deng, H. Liu and Z. Zhong, *Langmuir*, 2011, **28**, 2056–2065.

9 A. Kotyk and J. Slavík, *Intracellular pH and its Measurement*, CRC, 1989.

10 J. A. Thomas, R. N. Buchsbaum, A. Zimniak and E. Racker, *Biochemistry*, 1979, **18**, 2210–2218.

11 A. De Hemptinne, *J. Physiol.*, 1979, **295**, 5P.

12 V. V. Kupriyanov, B. Xiang, J. Sun, O. Jilkina and R. Deslauriers, *Biochim. Biophys. Acta, Mol. Basis Dis.*, 2002, **1586**, 57–70.

13 M. Vermathen, M. Marzorati, P. Vermathen and P. Bigler, *Langmuir*, 2010, **26**, 11085–11094.

14 G. Bright, G. Fisher, J. Rogowska and D. Taylor, *Methods Cell Biol.*, 1989, **30**, 157–192.

15 J. Han and K. Burgess, *Chem. Rev.*, 2010, **110**, 2709–2728.

16 S. Ogikubo, T. Nakabayashi, T. Adachi, M. S. Islam, T. Yoshizawa, M. Kinjo and N. Ohta, *J. Phys. Chem. B*, 2011, **115**, 10385–10390.

17 K. A. Giuliano and R. J. Gillies, *Anal. Biochem.*, 1987, **167**, 362–371.

18 C. C. Overly, K. D. Lee, E. Berthiaume and P. J. Hollenbeck, *Proc. Natl. Acad. Sci. U. S. A.*, 1995, **92**, 3156–3160.

19 N. Barrash-Shiftan, B. Brauer and E. Pines, *J. Phys. Org. Chem.*, 1998, **11**, 743–750.

20 T. Rink, R. Tsien and T. Pozzan, *J. Cell Biol.*, 1982, **95**, 189–196.

21 T. Speake and A. C. Elliott, *J. Physiol.*, 1998, **506**, 415–430.

22 I. Kurtz and R. S. Balaban, *Biophys. J.*, 1985, **48**, 499.

23 B. S. Gan, E. Krump, L. D. Shrode and S. Grinstein, *Am. J. Physiol.: Cell Physiol.*, 1998, **275**, C1158–C1166.

24 S. Sengupta, D. Eavarone, I. Capila, G. Zhao, N. Watson, T. Kiziltepe and R. Sasisekharan, *Nature*, 2005, **436**, 568–572.

25 A. K. Gupta and M. Gupta, *Biomaterials*, 2005, **26**, 3995–4021.

26 M.-H. Hsiao, T.-H. Tung, C.-S. Hsiao and D.-M. Liu, *Carbohydr. Polym.*, 2012, **89**, 632–639.

27 S.-H. Hu, B.-J. Liao, C.-S. Chiang, P.-J. Chen, I. W. Chen and S.-Y. Chen, *Adv. Mater.*, 2012, **24**, 3627–3632.

28 E. Lee, H. Kim, I. H. Lee and S. Jon, *J. Controlled Release*, 2009, **140**, 79–85.

29 T.-Y. Liu, S.-Y. Chen, Y.-L. Lin and D.-M. Liu, *Langmuir*, 2006, **22**, 9740–9745.

30 K.-H. Liu, S.-Y. Chen, D.-M. Liu and T.-Y. Liu, *Macromolecules*, 2008, **41**, 6511–6516.

31 Y.-J. Wang, Y.-C. Chien, C.-H. Wu and D.-M. Liu, *Mol. Pharm.*, 2011, **8**, 2339–2349.

32 Y.-J. Wang, H.-Y. Lin, C.-H. Wu and D.-M. Liu, *Mol. Pharm.*, 2012, **9**, 2268–2279.

33 N. A. Peppas, *Pharm. Acta Helv.*, 1985, **60**, 110–111.

34 P. Costa and J. M. Sousa Lobo, *Eur. J. Pharm. Sci.*, 2001, **13**, 123–133.

35 J. Griffiths, *Br. J. Cancer*, 1991, **64**, 425.

36 M. Schindler, S. Grabski, E. Hoff and S. M. Simon, *Biochemistry*, 1996, **35**, 2811–2817.

37 O. Seksek and J. Bolard, *J. Cell Sci.*, 1996, **109**, 257–262.

38 M. Aguedo, Y. Waché and J.-M. Belin, *FEMS Microbiol. Lett.*, 2001, **200**, 185–189.

This journal is © The Royal Society of Chemistry 2014

J. Mater. Chem. B, 2014, **2**, 6580–6589 | **6589**